



Cite this: DOI: 10.1039/c9ta10629d

Received 26th September 2019
Accepted 30th November 2019

DOI: 10.1039/c9ta10629d

rsc.li/materials-a

Photothermally assisted photocatalytic conversion of CO₂–H₂O into fuels over a WN–WO₃ Z-scheme heterostructure†

Dali Liu,^a You Xu,^a Mengyao Sun,^a Yi Huang,^a Yifu Yu ^{ab} and Bin Zhang ^{*ac}

CO₂ conversion into value-added fuels has been considered as a promising solution to solve environmental problems and energy crises. However, the efficiency of photocatalytic CO₂ conversion is low. In addition, infrared light in the solar spectrum is not utilized properly in most traditional photocatalytic reactions. Thus, the search for photocatalysts that exploit the wide solar spectrum to achieve an efficient water-based CO₂ conversion performance is still highly challenging. Herein, we construct a WN–WO₃ Z-scheme heterostructure to exploit the wide solar spectrum for efficient CO₂–H₂O conversion into fuels (H₂, CO, and CH₄) without any sacrificial agents. After 5 h irradiation, the yields of H₂, CO, and CH₄ are 3.0, 1.4, and 1.9 times higher than that of WN, respectively. The activity improvement is ascribed to the direct Z-scheme mechanism of the WN–WO₃ heterostructure under ultraviolet-visible illumination. In addition, the infrared light in sunlight is also utilized by the WN–WO₃ heterostructure to generate heat *via* photo-to-thermal conversion, which further accelerates such a conversion reaction. This work offers a unique perspective for designing transition metal nitride/oxide heterostructures and paves a new way to boost the CO₂-to-fuel conversion performance.

The solar-driven conversion of CO₂ into useful hydrocarbon fuels offers a sustainable way for solving environmental problems and energy crises.^{1–7} Extensive research efforts have been made to explore suitable semiconductor materials as efficient photocatalysts for CO₂ conversion.^{8–15} In particular, a variety of well-designed heterostructures have been designed to improve photoactivity *via* accelerating the charge-carrier separation.^{16–18}

However, the kinetic limitations of multiple e[−]/h⁺ transfer processes and the thermodynamically stable CO₂ molecules lead to low efficiency of photocatalytic CO₂ conversion, thus restricting its practical applications.^{19–21} Thus, to further improve the efficiency, photothermal CO₂ conversion has been explored as a promising strategy due to the high efficiency of photo-to-heat conversion.^{22,23} However, H₂ is often required for most photothermal conversion methods. Currently, approximately 95% of total H₂ is obtained from the steam reforming of natural gas accompanied with unwanted CO₂ emissions. A new research trend in this field is to directly utilize hydrogen atoms generated from water splitting as hydrogen resources for CO₂ conversion.^{24–28} Nevertheless, most previously reported studies have been performed under harsh conditions (*e.g.*, external heating, high pressure, and UV illumination). Recently, the photothermal effect of carbon-based materials has been reported to promote photocatalytic CO₂ conversion.^{29–31} For instance, Wang *et al.* demonstrated the remarkable photothermal effect of graphene on photocatalytic CO₂ reduction. However, the photothermal effect of other non-carbon-based materials on photocatalytic CO₂ conversion has been rarely studied. In addition, ultraviolet-visible light is mainly used in traditional photothermal reactions, while the infrared light in the solar spectrum is not utilized completely.³² Therefore, there is an urgent need to look for photocatalysts that can exploit the wide solar spectrum to achieve an efficient water-based CO₂ conversion performance in the absence of sacrificial agents under mild conditions.

Semiconducting nitrides are a promising class of inorganic materials for solar energy conversion applications as they have better solar absorption and electrical transport properties than the more widely studied oxides.^{33–35} The construction of Z-scheme semiconductor-based heterostructures represents a powerful strategy to enhance the efficiency of photocatalysis-based reactions.^{36–42} However, semiconducting nitride-based Z-scheme heterostructures for CO₂ conversion, especially in combination with the thermal effect, still remain untouched. Thus, the rational design of metal nitride-based Z-scheme

^aTianjin Key Laboratory of Molecular Optoelectronic Sciences, Department of Chemistry, School of Science, Tianjin University, Tianjin 300072, China. E-mail: bzhang@tju.edu.cn

^bInstitute of Molecular Plus, Tianjin University, Tianjin 300072, China

^cCollaborative Innovation Center of Chemical Science and Engineering, Tianjin 300072, China

† Electronic supplementary information (ESI) available: Experimental details, supplementary characterization and electrochemical measurements. See DOI: 10.1039/c9ta10629d

heterostructures for an efficient CO₂ conversion performance is highly desirable.

Herein, we report the synthesis of a WN-WO₃ Z-scheme heterostructure by the *in situ* partial thermal oxidation of WN (Fig. 1a). WN was partially *in situ* converted into WO₃ on the surface, allowing the construction of a Z-scheme photocatalyst. The WN-WO₃ Z-scheme heterostructure exploited the wide solar spectrum to achieve outstanding activity for the photo-thermally assisted photocatalytic conversion of CO₂-H₂O into fuels (H₂, CO, and CH₄) without external sacrificial agents (Fig. 1b). The superior performance of WN-WO₃ was attributed to the direct Z-scheme photocatalytic mechanism. Meanwhile, as the main component of the WN-WO₃ heterostructure, WN could absorb almost the whole spectrum of solar light because of its narrow band gap. Although the absorbed sunlight could not be directly used to produce active electrons or holes for the photocatalytic reaction, it could increase the temperature of the WN-WO₃ heterostructure to create a local photothermal effect. The local photothermal effect is beneficial for accelerating the reactant adsorption-desorption and charge carrier migration on the WN-WO₃ heterostructure, thus enhancing the efficiency of photocatalytic CO₂ conversion.

WN nanorods were synthesized *via* the complete nitridation of WO₃ (ESI[†]).⁴³ The scanning electron microscopy (SEM) and transmission electron microscopy (TEM) images in Fig. S1[†] reveal that WN preserves the nanorod-like morphology of WO₃. The lattice fringe of 0.24 nm in Fig. S1b[†] is indexed to the WN (111) plane. Then, the heterostructure was *in situ* formed by the partial thermal oxidation of WN. The SEM and TEM images show that the product still preserves the nanorod-like morphology after oxidation treatment (Fig. 2a and inset in Fig. 2b). Differing from initial WN, some amorphous regions were observed in the high-resolution TEM (HRTEM) image (noted by blue circles in Fig. 2b) after the oxidation treatment. As a result, the intensities of the WN (JCPDS no. 65-2898) diffraction peaks in the XRD patterns decreased after the oxidation treatment (Fig. 2c), suggesting a decrease in the WN content and an increase in the amorphous regions.⁴⁴ To confirm the components of amorphous regions, the products were further crystallized in an Ar atmosphere at 500 °C (denoted as Cryst). As shown in Fig. 2c, the additional XRD peaks of the sample after crystallization can be attributed to WO₃ (JCPDS no. 46-1096), revealing that the initial amorphous component is

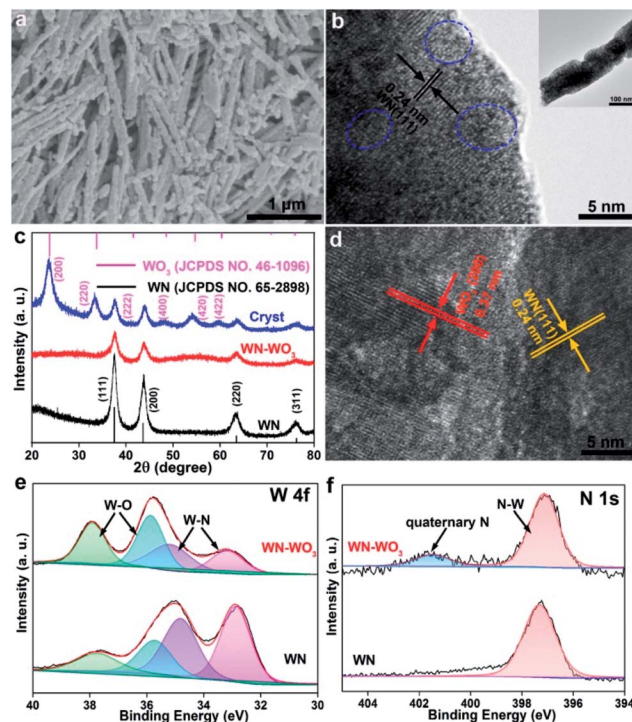


Fig. 2 (a) SEM and (b) HRTEM (inset: TEM) images of WN-WO₃. (c) XRD patterns of WN (black), WN-WO₃ (red) and crystallized WN-WO₃ (blue). (d) HRTEM image of crystallized WN-WO₃. (e and f) XPS spectra of W 4f and N 1s for WN and WN-WO₃.

WO₃.⁴⁵ Moreover, the lattice fringe of 0.37 nm, indexed to the WO₃ (200) plane, is observed in the HRTEM image of the crystallized sample (Fig. 2d). Thus, the WN-WO₃ heterostructure is successfully obtained *via* the thermal oxidation treatment. The CO₂ chemical adsorption capacities of WN and the WN-WO₃ heterostructure were investigated by CO₂ temperature-programmed desorption (CO₂-TPD). In Fig. S2a,[†] there are two types of desorption peaks, which represent weak CO₂ adsorption (peak I, 60–100 °C) and strong CO₂ adsorption (peak II, 300–500 °C), respectively. Compared with the observation for WN, the II peaks of WN-WO₃ shifted to a higher temperature, suggesting stronger CO₂ adsorption.⁴⁶ Meanwhile, as shown in Table S1,[†] the amount of strong CO₂ adsorption is largely enhanced in the WN-WO₃ heterostructure. The amount of weak CO₂ adsorption (peak I) was very small and could be ignored. Therefore, it could be proposed that the WN-WO₃ heterostructure exhibited better CO₂ chemical adsorption capacity. Fig. S2b[†] shows the water vapor adsorption/desorption isotherms of WN and the WN-WO₃ heterostructure. Compared with the observation for WN, the adsorption capacity of WN-WO₃ to water vapor decreased. This resulted from the formation of WO₃, whose adsorption capacity to water vapor was poor. X-ray photoelectron spectroscopy (XPS) was carried out to analyze the chemical components of WN and the WN-WO₃ heterostructure. The survey spectra (Fig. S3[†]) show a weak O 1s peak for WN due to the inevitable exposure to air before XPS measurements;^{47,48} in contrast, fresh WN was used for the photocatalytic tests. In the W 4f spectra (Fig. 2e), two

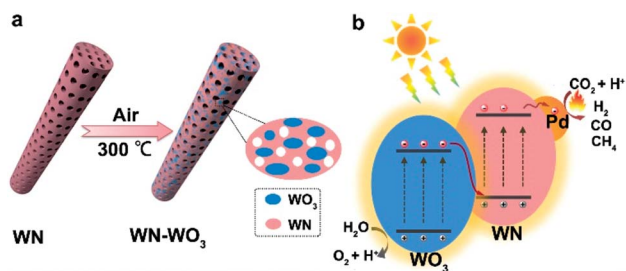


Fig. 1 (a) Scheme illustrating the synthetic process of the WN-WO₃ heterostructure. (b) Z-scheme diagram of Pd-loaded WN-WO₃ heterostructure for CO₂-H₂O conversion.

characteristic peaks of the W–N bond are located at 33.5 and 35.1 eV.³⁴ Besides, the peaks at 35.9 and 37.8 eV are attributed to the W–O bond.⁴⁹ It is straightforward that the intensity of the W–O bond increases after the oxidation treatment due to the increased oxide content. As a result, the intensity of the W–N bond is reduced. As shown for the N 1s spectra in Fig. 2f, the characteristic peak of the N–W bond is located at 397.4 eV for WN.⁵⁰ Compared with WN, WN–WO₃ shows another peak at 401.7 eV, which is associated with the N atoms at the tetrahedral interstitial sites.⁵¹ In addition, the N–O bond was not observed in WN–WO₃. Thus, the WN–WO₃ heterostructure rather than oxygen-doped WN was obtained. More importantly, the *in situ*-formed WO₃ could maintain excellent mechanical and electrical interconnection with neighboring WN, which favored the formation of a junction between the two semiconductors and facilitated photo-induced charge-carrier separation and migration during photocatalysis.

CO₂–H₂O conversion was performed in a home-made sealed reaction chamber. Fig. 3a shows the CO₂ reduction yields for the Pd-loaded WN–WO₃ heterostructure after 5 h irradiation. XPS analysis demonstrated that the Pd element was present in the form of metallic palladium (Fig. S4†). In addition, the actual content of Pd was 0.93%. As control samples, Pd-loaded WN and WO₃ were also tested. The CO₂ reduction yields of H₂, CO, and CH₄ for WN were 605.2 ± 7.8, 52.7 ± 1.4, and 107.5 ± 3.2 μmol g⁻¹, respectively. Compared with WN, WN–WO₃ exhibited a better performance. The yields of H₂, CO, and CH₄ reached 1842.6 ± 14.1, 75.8 ± 1.4, and 202.7 ± 3.8 μmol g⁻¹, which were 3.0, 1.4, and 1.9 times that of WN, respectively. The formation rates of H₂, CO, and CH₄ for WN–WO₃ reached 368.5 ± 2.8, 15.2 ± 0.3, and 40.6 ± 0.7 μmol h⁻¹ g⁻¹, respectively (Fig. 3b). In general, the total consumed electron number (TCEN) for CO₂ conversion is often used to estimate CO₂ reduction efficiency due to the complexity of the products. The TCEN of the WN–WO₃ heterostructure was higher than that of CdS–WO₃,¹⁴ N-doped WO_{3-x},⁴⁸ and many other photocatalysts (Table S2†). To investigate the effect of Pd on the performance, we carried

out CO₂ conversion experiments on as-prepared WN–WO₃ as well as on the Pd-loaded WN–WO₃ heterostructure (Fig. S5†). For both samples, the major products observed were H₂, CO, and CH₄. It was seen that the yields of H₂, CO, and CH₄ increased from 500.9, 64.3, and 112.7 μmol g⁻¹ over the WN–WO₃ heterostructure to 2113.1, 78.4, and 213.5 μmol g⁻¹ over the Pd-loaded WN–WO₃ heterostructure. Thus, Pd nanoparticles as co-catalysts not only enhanced the photocatalytic efficiency of CO₂ conversion but also increased the selectivity of CH₄. To demonstrate the overall photocatalytic mechanism, the evolution rate of oxygen as the oxidation product was measured (Fig. S6†). The result displayed in Fig. S6† shows that the electrons from water oxidation are almost comparable to the consumed electrons for the reduction reaction on both WN and WN–WO₃. This result clearly demonstrated that H₂O acted as an electron donor in the whole photocatalytic process.⁵² To evaluate the stability, WN–WO₃ was repeatedly used for 5 cycles, and no obvious deactivation was observed (Fig. 3c). In addition, the good morphological and structural stabilities of WN–WO₃ were confirmed by the SEM, XRD, and XPS results obtained after long-term photocatalytic tests (Fig. S7 and S8†), thus confirming the good stability of the WN–WO₃ heterostructure. The ¹³CO₂ isotopic tracer experiments (Fig. 3d) demonstrated that the carbon atoms of the produced CO and CH₄ stemmed from the CO₂ feedstock. Additionally, *in situ* diffuse reflectance infrared Fourier transform spectroscopy (DRIFTS) analysis (Fig. S9†) demonstrated that these adsorbed CO₂ and H₂O were converted into carbonate, HCOO, HCHO, and CH₃O before their transformation into CO and CH₄ under UV light irradiation.⁵³

To demonstrate the effect of light intensity on activity, we tested the CO₂–H₂O reduction performance of the Pd-loaded WN–WO₃ heterostructure under simulated sunlight irradiation with different intensities (Fig. S10†). With the light intensity increasing, the yield of H₂ increased from 1.1 mmol g⁻¹ (light intensity: 200 mW cm⁻²) to 13.3 mmol g⁻¹ (light intensity: 800 mW cm⁻²). In addition, the yields of CO and CH₄ increased from 69.7 and 84.7 μmol g⁻¹ (light intensity: 200 mW cm⁻²) to 681.5 and 670.1 μmol g⁻¹ (light intensity: 800 mW cm⁻²), respectively. Thus, the rate of H₂, CO, and CH₄ formation increased with the intensity of light. In addition, the selectivities for CH₄ and CO were the best at 400 and 800 mW cm⁻², respectively.

In order to study the effect of the different wavelengths of light on the catalytic process, we measured the transient photocurrent response of the Pd-loaded WN–WO₃ heterostructure under ultraviolet, visible, and infrared light irradiation (Fig. 4a). The intensity of all three lights was maintained at 0.4 W cm⁻². Fig. 4a shows that there are obvious photocurrent responses of the Pd-loaded WN–WO₃ heterostructure under ultraviolet and visible light irradiation, whereas no obvious photocurrent response can be observed under infrared light irradiation. Meanwhile, the intensity of the photocurrent under UV light irradiation was higher than that under visible light irradiation. This revealed that both UV and visible lights could produce photogenerated carriers on the surface of the Pd-loaded WN–WO₃ heterostructure. In addition, the separation efficiency of photogenerated carriers on the Pd-loaded WN–

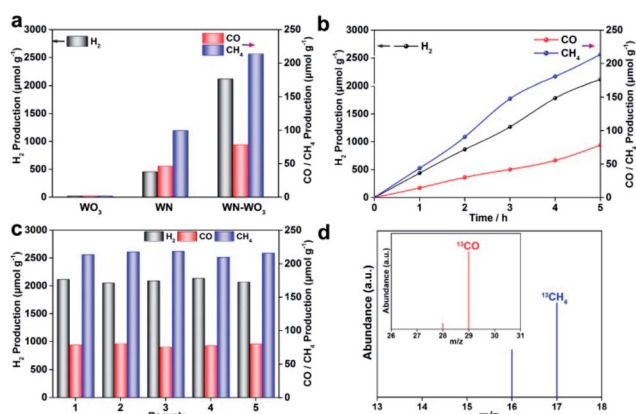


Fig. 3 (a) CO₂ conversion performance of WO₃, WN, and WN–WO₃ with Pd loading under simulated sunlight irradiation for 5 h. (b) The WN–WO₃ production of H₂, CO and CH₄ as a function of time. (c) The stability test of WN–WO₃ heterostructure. (d) The results of mass spectrometry in the ¹³CO₂ isotopic tracer experiment.

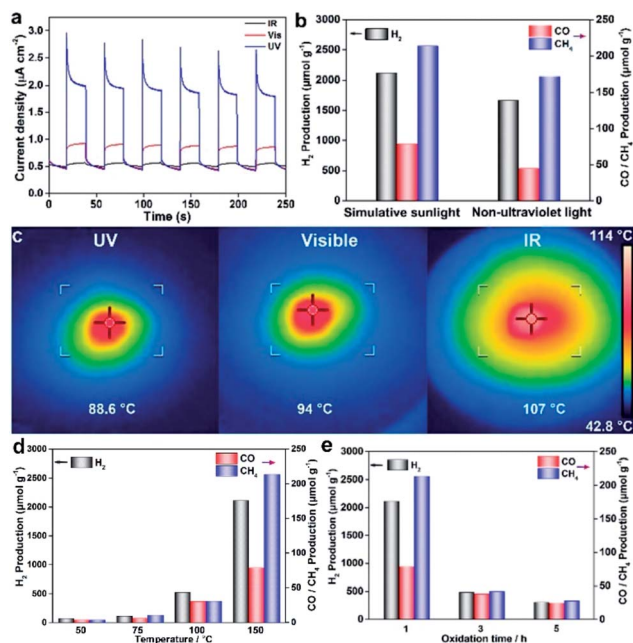


Fig. 4 (a) The transient photocurrent response of the Pd-loaded WN-WO₃ heterostructure under ultraviolet, visible and infrared light irradiation. (b) The CO₂-H₂O conversion performance of the Pd-loaded WN-WO₃ heterostructure under simulated sunlight and non-ultraviolet light irradiation for 5 h. (c) Infrared thermography images of the Pd-loaded WN-WO₃ heterostructure under ultraviolet, visible and infrared light irradiation. (d) The CO₂-H₂O reduction performances of the Pd-loaded WN-WO₃ heterostructure at different temperatures. (e) Performance comparison of the Pd-loaded WN-WO₃ heterostructures with different oxidation times.

WO₃ heterostructure under ultraviolet light was higher than that under visible light. To further investigate the effect of UV light on the performance, we compared the CO₂-H₂O conversion performance of the Pd-loaded WN-WO₃ heterostructure under simulated sunlight (wavelength: 200–1100 nm) and non-ultraviolet light (wavelength: 420–1100 nm) irradiation (Fig. 4b). The intensity of light was maintained at 0.4 W cm⁻². Compared with the observations for simulated sunlight irradiation, the yields of H₂, CO, and CH₄ declined under non-ultraviolet light. Thus, the efficiency was also reduced under non-ultraviolet light irradiation. To study the role of infrared light, we analyzed the infrared thermal images of the Pd-loaded WN-WO₃ heterostructure under UV, visible, and IR light irradiation with the same intensity (Fig. 4c). The temperatures of the Pd-loaded WN-WO₃ heterostructure under UV, visible, and IR light irradiation reached 88.6, 94, and 107 °C, respectively. Thus, the IR light contributed more to photo-to-thermal conversion. During the performance test, the temperature of the Pd-loaded WN-WO₃ heterostructure quickly reached 154 °C in 10 s under simulated solar light irradiation (Fig. S11†). We tested the CO₂ reduction performances of the Pd-loaded WN-WO₃ heterostructure at different temperatures (Fig. 4d). The photocatalyst was surrounded by circulating water in a jacketed reactor to adjust the temperature. The actual temperature on the surface of the photocatalyst was measured using an infrared camera.

With the reaction temperature decreasing, the yields of H₂, CO, and CH₄ experienced remarkable reduction. The temperature-dependent kinetic experiment on the photocatalytic CO₂ conversion was carried out to further investigate the role of heat.³¹ The rate constant for the overall reaction could be estimated using a pseudo-zero order model due to the dominant electron consumption selectivity and linear increase in CH₄ production. Fig. S12† presents the Arrhenius plot based on the kinetic experiments by varying the reaction temperature (50, 75, 100 and 150 °C) on the photocatalyst surface. The apparent activation energy value of the overall reaction over the Pd/WN-WO₃ heterostructure was calculated to be 46.9 kJ mol⁻¹. This result clearly explains that the elevation of surface temperature has a positive effect on CO₂ conversion. It can be inferred that the local photothermal effect will enhance the movement of gas molecules and charge carriers, contributing to improved CO₂ conversion efficiency. In addition, a series of control experiments were carried out (Table S3†). The temperature of a sample was varied by electric heating in the dark. No products could be detected in the dark situation, indicating the photocatalytic nature of our conversion reaction. The results of the control experiment in the Ar atmosphere further confirmed that the carbon sources of evolved CO and CH₄ are from CO₂ molecules. Thus, the CO₂-H₂O conversion reaction over the Pd-loaded WN-WO₃ heterostructure was driven by the photocatalysis under ultraviolet-visible light and accelerated by the photo-to-thermal conversion under infrared light. Fig. 4e exhibits the performance of the Pd-loaded WN-WO₃ heterostructures with different oxidation times. WN-WO₃ obtained by 1 h oxidation treatment showed the best performance among these catalysts. With the increase in the oxidation time, the activity of the WN-WO₃ heterostructure decreased due to the excessively thick oxide layer.

To reveal the reason for the enhanced CO₂ conversion performance of the WN-WO₃ heterostructure, a series of experiments were carried out. The band edge positions of WN and WO₃ were determined by UV-vis-NIR diffuse reflectance spectra (DRS) and ultraviolet photoelectron spectroscopy (UPS). The band gap (E_g) values of WN and WO₃ were calculated to be 1.9 and 2.4 eV, respectively (Fig. S13a and b†).⁵⁴ Moreover, the conduction band energy, E_c , of WN was estimated to be 4.03 eV by UPS analysis. Thus, the conduction band (CB) and valence band (VB) positions of WN were approximately -0.82 and +1.08 V *versus* a normal hydrogen electrode (NHE), respectively.⁵⁵ Similarly, the CB and VB positions of WO₃ were deduced at 0.63 and +3.03 V, respectively (Fig. S13c and d†). By combining these data, the corresponding band structure diagram could be schemed and a staggered band alignment heterostructure was constructed, as shown in Fig. 5a. To elucidate the interfacial charge migration in the WN-WO₃ heterostructure with the type-II or Z-scheme pathway, electron spin resonance (ESR) analysis was performed.⁵⁶ In detail, the semiconductors with the VB potential higher than 2.4 V *vs.* NHE could produce [•]OH radicals through the reaction of OH⁻/H₂O with the photogenerated holes. Thus, no obvious [•]OH signal was detected in WN due to the low VB potential (Fig. 5b). Compared with WO₃, WN-WO₃ showed a stronger DMPO-[•]OH

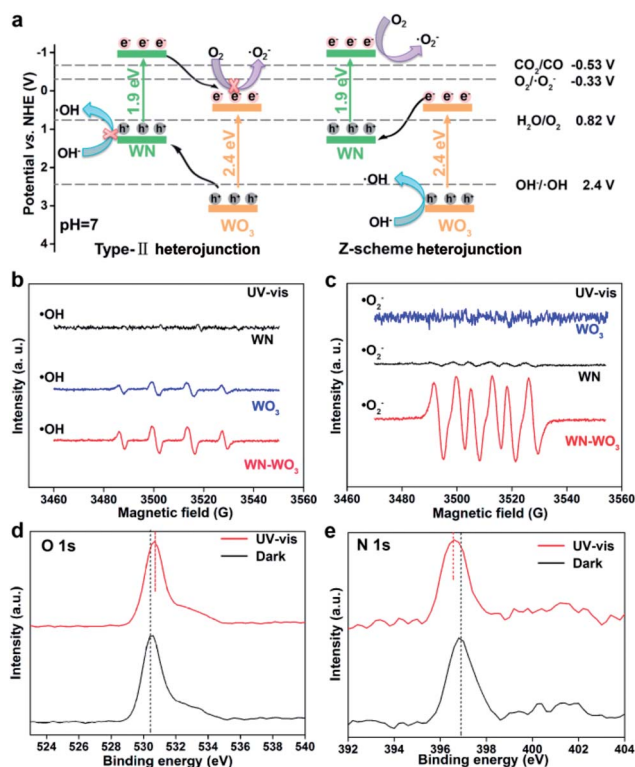


Fig. 5 (a) Schematic illustration of the charge-carrier migration mechanism according to the type-II and Z-scheme heterojunction for the WN–WO₃. (b) DMPO spin-trapping ESR spectra recorded for ·OH and (c) ·O₂⁻ under UV-vis light for WO₃, WN, and WN–WO₃. (d) O 1s and (e) N 1s XPS spectra of WN–WO₃ in the dark and UV-vis light irradiation.

adduct signal with the relative intensities of 1 : 2 : 2 : 1, suggesting that the photogenerated holes of WN–WO₃ accumulated on the VB of WO₃. Similarly, considering the fact that the CB potential of WO₃ was more positive than the standard potential of O₂*/O₂⁻ (–0.33 V vs. NHE), no obvious DMPO–·O₂⁻ (DMPO = 5,5-dimethyl-1-pyrroline *N*-oxide) signal was observed for WO₃ (Fig. 5c). The enhanced ·O₂⁻ signal for WN–WO₃ demonstrates that the photogenerated electrons of the heterostructure accumulate on the CB of WN, confirming the Z-scheme mechanism with superior charge separation efficiency. To further validate the Z-scheme mechanism, *in situ* irradiated XPS was carried out (Fig. 5d and e).^{57,58} Under UV-vis light irradiation, the O 1s and N 1s peaks showed positive (by 0.1 eV) and negative shifts (by –0.2 eV), respectively, in comparison with those under a dark condition. This implied that the electron density decreased on WO₃ and increased on WN. Therefore, the photogenerated electrons of WN–WO₃ migrated from WO₃ to WN, following the proposed Z-scheme mechanism instead of a type-II heterojunction mechanism. The transient photocurrent response measurements (Fig. S14†) directly indicated that WN–WO₃ showed higher separation efficiency for the photogenerated charge carriers compared with WN. Photoluminescence (PL) was used to explore the carrier separation of WN and the WN–WO₃ heterostructure. The PL spectra of WN and the WN–WO₃ heterostructure in the wavelength range of

390–600 nm are shown in Fig. S15a.† Obviously, WN emitted strong PL signals with peaks at 408, 432, and 459 nm. Compared with the observation for WN, the PL signal intensity of the WN–WO₃ heterostructure significantly decreased, indicating a much lower recombination rate of photogenerated electrons and holes. The PL results revealed that the WN–WO₃ heterostructure showed higher photogenerated electron-hole separation efficiency. The separation behaviors of the photogenerated carriers were further confirmed by lifetime analysis based on the fluorescence decay shown in Fig. S15b.† The average lifetime of WN–WO₃ was longer than that of WN, suggesting more effective separation and migration of the photogenerated carriers in the WN–WO₃ heterostructure.⁵⁹ Thus, the WN–WO₃ Z-scheme heterostructure exhibited a promising CO₂ conversion performance.

Conclusions

In conclusion, we successfully synthesized a WN–WO₃ heterostructure as a direct Z-scheme catalyst that could exploit the wide solar spectrum for the photothermally assisted photocatalytic conversion of CO₂–H₂O. The Pd-loaded WN–WO₃ heterostructure exhibited excellent activities for the conversion of CO₂–H₂O into H₂ (368.5 ± 2.8 μmol h⁻¹ g⁻¹), CO (15.2 ± 0.3 μmol h⁻¹ g⁻¹), and CH₄ (40.6 ± 0.7 μmol h⁻¹ g⁻¹), which were much higher than those of WO₃ and WN. The activity improvement was ascribed to the improved photoinduced carrier separation and migration efficiency in the WN–WO₃ heterostructure due to the Z-scheme charge transfer mode under stimulated sunlight irradiation. Meanwhile, the conversion of CO₂–H₂O into fuels could also be facilitated by heat generated from the photo-to-thermal effect. This work offers a stepping stone to design transition metal nitride/oxide heterogeneous nanostructures and paves a new avenue to boost the performance of photothermally assisted photocatalysis for water splitting, CO₂-to-fuel conversion, and organic synthesis.

Conflicts of interest

The authors declare no competing financial interest.

Acknowledgements

We acknowledge the financial support from the National Natural Science Foundation of China (No. 21871206 and No. 21422104) and the Natural Science Foundation of Tianjin City (No. 17JCJQC44700).

Notes and references

- M. Schreier, F. Héroguel, L. Steier, S. Ahmad, J. S. Luterbacher, M. T. Mayer, J. Luo and M. Grätzel, *Nat. Energy*, 2017, 2, 17087.
- Y. Ji and Y. Luo, *J. Am. Chem. Soc.*, 2016, 138, 15896–15902.
- J. Ran, M. Jaroniec and S. Z. Qiao, *Adv. Mater.*, 2018, 30, 1704649.

- 4 Y. F. Xu, M. Z. Yang, B. X. Chen, X. D. Wang, H. Y. Chen, D. B. Kuang and C. Y. Su, *J. Am. Chem. Soc.*, 2017, **139**, 5660–5663.
- 5 P. Xia, M. Antonietti, B. Zhu, T. Heil, J. Yu and S. Cao, *Adv. Funct. Mater.*, 2019, **29**, 1900093.
- 6 T. Ouyang, H. J. Wang, H. H. Huang, J. W. Wang, S. Guo, W. J. Liu, D. C. Zhong and T. B. Lu, *Angew. Chem., Int. Ed.*, 2018, **57**, 16480–16485.
- 7 K. D. Yang, Y. Ha, U. Sim, J. An, C. W. Lee, K. Jin, Y. Kim, J. Park, J. S. Hong, J. H. Lee, H. E. Lee, H. Y. Jeong, H. Kim and K. T. Nam, *Adv. Funct. Mater.*, 2016, **26**, 233–242.
- 8 J. Di, C. Zhu, M. Ji, M. Duan, R. Long, C. Yan, K. Gu, J. Xiong, Y. She, J. Xia, H. Li and Z. Liu, *Angew. Chem., Int. Ed.*, 2018, **57**, 14847–14851.
- 9 C. Gao, Q. Meng, K. Zhao, H. Yin, D. Wang, J. Guo, S. Zhao, L. Chang, M. He, Q. Li, H. Zhao, X. Huang, Y. Gao and Z. Tang, *Adv. Mater.*, 2016, **28**, 6485–6490.
- 10 S. Wang, B. Y. Guan, Y. Lu and X. W. D. Lou, *J. Am. Chem. Soc.*, 2017, **139**, 17305–17308.
- 11 C. Cometto, R. Kuriki, L. Chen, K. Maeda, T. C. Lau, O. Ishitani and M. Robert, *J. Am. Chem. Soc.*, 2018, **140**, 7437–7440.
- 12 Y. Wang, Z. Zhang, L. Zhang, Z. Luo, J. Shen, H. Lin, J. Long, J. C. S. Wu, X. Fu, X. Wang and C. Li, *J. Am. Chem. Soc.*, 2018, **140**, 14595–14598.
- 13 M. Ou, W. Tu, S. Yin, W. Xing, S. Wu, H. Wang, S. Wan, Q. Zhong and R. Xu, *Angew. Chem.*, 2018, **130**, 13758–13762.
- 14 J. Jin, J. Yu, D. Guo, C. Cui and W. Ho, *Small*, 2015, **11**, 5262–5271.
- 15 S. Yang, W. Hu, X. Zhang, P. He, B. Pattengale, C. Liu, M. Cendejas, I. Hermans, X. Zhang, J. Zhang and J. Huang, *J. Am. Chem. Soc.*, 2018, **140**, 14614–14618.
- 16 X. Hong, J. Kim, S. F. Shi, Y. Zhang, C. Jin, Y. Sun, S. Tongay, J. Wu, Y. Zhang and F. Wang, *Nat. Nanotechnol.*, 2014, **9**, 682.
- 17 K. X. Zhang, H. Su, H. H. Wang, J. J. Zhang, S. Y. Zhao, W. Lei, X. Wei, X. H. Li and J. S. Chen, *Adv. Sci.*, 2018, **5**, 1800062.
- 18 T. Butburee, Z. Sun, A. Centeno, F. Xie, Z. Zhao, D. Wu, P. Peerakiatkhajohn, S. Thaweesak, H. Wang and L. Wang, *Nano Energy*, 2019, **62**, 426–433.
- 19 Z. Sun, N. Talreja, H. Tao, J. Texter, M. Muhler, J. Strunk and J. Chen, *Angew. Chem., Int. Ed.*, 2018, **57**, 7610–7627.
- 20 X. Cui, J. Wang, B. Liu, S. Ling, R. Long and Y. Xiong, *J. Am. Chem. Soc.*, 2018, **140**, 16514–16520.
- 21 Z. j. Wang, H. Song, H. Liu and J. Ye, *Angew. Chem., Int. Ed.*, 2019, DOI: 10.1002/anie.201907443.
- 22 P. G. O'Brien, K. K. Ghuman, A. A. Jelle, A. Sandhel, T. E. Wood, J. Y. Y. Loh, J. Jia, D. Perovic, C. V. Singh, N. P. Kherani, C. A. Mims and G. A. Ozin, *Energy Environ. Sci.*, 2018, **11**, 3443–3451.
- 23 G. Chen, R. Gao, Y. Zhao, Z. Li, G. I. N. Waterhouse, R. Shi, J. Zhao, M. Zhang, L. Shang, G. Sheng, X. Zhang, X. Wen, L. Z. Wu, C. H. Tung and T. Zhang, *Adv. Mater.*, 2018, **30**, 1704663.
- 24 Y. X. Pan, Y. You, S. Xin, Y. Li, G. Fu, Z. Cui, Y. L. Men, F. F. Cao, S. H. Yu and J. B. Goodenough, *J. Am. Chem. Soc.*, 2017, **139**, 4123–4129.
- 25 J. Di, X. Zhao, C. Lian, M. Ji, J. Xia, J. Xiong, W. Zhou, X. Cao, Y. She, H. Liu, K. P. Loh, S. J. Pennycook, H. Li and Z. Liu, *Nano Energy*, 2019, **61**, 54–59.
- 26 C. Liu, B. C. Colón, M. Ziesack, P. A. Silver and D. G. Nocera, *Science*, 2016, **352**, 1210.
- 27 M. Li, L. Zhang, M. Wu, Y. Du, X. Fan, M. Wang, L. Zhang, Q. Kong and J. Shi, *Nano Energy*, 2016, **19**, 145–155.
- 28 Y. Wang, N. Y. Huang, J. Q. Shen, P. Q. Liao, X. M. Chen and J. P. Zhang, *J. Am. Chem. Soc.*, 2018, **140**, 38–41.
- 29 J. Low, L. Zhang, T. Tong, B. Shen and J. Yu, *J. Catal.*, 2018, **361**, 255–266.
- 30 W. Wang, D. Xu, B. Cheng, J. Yu and C. Jiang, *J. Mater. Chem. A*, 2017, **5**, 5020–5029.
- 31 M. Xu, X. Hu, S. Wang, J. Yu, D. Zhu and J. Wang, *J. Catal.*, 2019, **377**, 652–661.
- 32 J. Ren, S. Ouyang, H. Xu, X. Meng, T. Wang, D. Wang and J. Ye, *Adv. Energy Mater.*, 2017, **7**, 1601657.
- 33 M. G. Kibria, F. A. Chowdhury, S. Zhao, B. Alotaibi, M. L. Trudeau, H. Guo and Z. Mi, *Nat. Commun.*, 2015, **6**, 6797.
- 34 Y. L. Wang, T. Nie, Y. H. Li, X. L. Wang, L. R. Zheng, A. P. Chen, X. Q. Gong and H. G. Yang, *Angew. Chem., Int. Ed.*, 2017, **56**, 7430–7434.
- 35 A. Zakutayev, *J. Mater. Chem. A*, 2016, **4**, 6742–6754.
- 36 C. Zhou, S. Wang, Z. Zhao, Z. Shi, S. Yan and Z. Zou, *Adv. Funct. Mater.*, 2018, **28**, 1801214.
- 37 S. Hua, D. Qu, L. An, W. Jiang, Y. Wen, X. Wang and Z. Sun, *Appl. Catal., B*, 2019, **240**, 253–261.
- 38 A. Iwase, S. Yoshino, T. Takayama, Y. H. Ng, R. Amal and A. Kudo, *J. Am. Chem. Soc.*, 2016, **138**, 10260–10264.
- 39 C. Dong, S. Lu, S. Yao, R. Ge, Z. Wang, Z. Wang, P. An, Y. Liu, B. Yang and H. Zhang, *ACS Catal.*, 2018, **8**, 8649–8658.
- 40 M. Kobayashi, S. Masaoka and K. Sakai, *Angew. Chem., Int. Ed.*, 2012, **51**, 7431–7434.
- 41 Q. Wang, T. Hisatomi, Y. Suzuki, Z. Pan, J. Seo, M. Katayama, T. Minegishi, H. Nishiyama, T. Takata, K. Seki, A. Kudo, T. Yamada and K. Domen, *J. Am. Chem. Soc.*, 2017, **139**, 1675–1683.
- 42 B. Zhao, Y. Huang, D. Liu, Y. Yu and B. Zhang, *Sci. China: Chem.*, 2019, DOI: 10.1007/s11426-019-9620-1.
- 43 S. Jing, L. Luo, S. Yin, F. Huang, Y. Jia, Y. Wei, Z. Sun and Y. Zhao, *Appl. Catal., B*, 2014, **147**, 897–903.
- 44 Y. Yi, L. Yu, Z. Tian, Y. Song, Y. Shao, L. Gao, J. Sun and Z. Liu, *Adv. Funct. Mater.*, 2018, **28**, 1805510.
- 45 M. S. Kim, E. Lim, S. Kim, C. Jo, J. Chun and J. Lee, *Adv. Funct. Mater.*, 2017, **27**, 1603921.
- 46 Y. Zhao, Y. Wei, X. Wu, H. Zheng, Z. Zhao, J. Liu and J. Li, *Appl. Catal., B*, 2018, **226**, 360–372.
- 47 H. Yu, X. Yang, X. Xiao, M. Chen, Q. Zhang, L. Huang, J. Wu, T. Li, S. Chen, L. Song, L. Gu, B. Y. Xia, G. Feng, J. Li and J. Zhou, *Adv. Mater.*, 2018, **30**, 1805655.
- 48 Y. Zhu, G. Chen, Y. Zhong, W. Zhou and Z. Shao, *Adv. Sci.*, 2018, **5**, 1700603.
- 49 D. Liu, C. Wang, Y. Yu, B. H. Zhao, W. Wang, Y. Du and B. Zhang, *Chem*, 2019, **5**, 376–389.
- 50 X. Cui, Z. Pan, L. Zhang, H. Peng and G. Zheng, *Adv. Energy Mater.*, 2017, **7**, 1701456.

- 51 H. Yan, C. Tian, L. Wang, A. Wu, M. Meng, L. Zhao and H. Fu, *Angew. Chem., Int. Ed.*, 2015, **54**, 6325–6329.
- 52 S. Wang, M. Xu, T. Peng, C. Zhang, T. Li, I. Hussain, J. Wang and B. Tan, *Nat. Commun.*, 2019, **10**, 676.
- 53 J. Low, L. Zhang, B. Zhu, Z. Liu and J. Yu, *ACS Sustainable Chem. Eng.*, 2018, **6**, 15653–15661.
- 54 X. Jiao, Z. Chen, X. Li, Y. Sun, S. Gao, W. Yan, C. Wang, Q. Zhang, Y. Lin, Y. Luo and Y. Xie, *J. Am. Chem. Soc.*, 2017, **139**, 7586–7594.
- 55 J. Liu, Y. Liu, N. Liu, Y. Han, X. Zhang, H. Huang, Y. Lifshitz, S. T. Lee, J. Zhong and Z. Kang, *Science*, 2015, **347**, 970.
- 56 Z. Jiang, W. Wan, H. Li, S. Yuan, H. Zhao and P. K. Wong, *Adv. Mater.*, 2018, **30**, 1706108.
- 57 J. Low, B. Dai, T. Tong, C. Jiang and J. Yu, *Adv. Mater.*, 2019, **31**, 1802981.
- 58 X. Liu, G. Dong, S. Li, G. Lu and Y. Bi, *J. Am. Chem. Soc.*, 2016, **138**, 2917–2920.
- 59 Y. Liu, C. Miao, P. Yang, Y. He, J. Feng and D. Li, *Appl. Catal., B*, 2019, **244**, 919–930.